



Effect of the Particles Morphology on the Electrochemical Performance of $\text{Na}_3\text{V}_2(\text{PO}_4)_2\text{F}_{3-y}\text{O}_y$

Runhe Fang,^[a, d] Jacob Olchowka,^{*,[b, d, e]} Chloé Pablos,^[b, c, d] Paula Sanz Camacho,^[b] Dany Carlier,^[b, d, e] Laurence Croguennec,^[b, d, e] and Sophie Cassaignon^{*,[a, d]}

Among all the positive electrode materials explored for Na-ion batteries, the family of $\text{Na}_3\text{V}^{3+}_{2-y}(\text{V}^{4+}\text{O})_y(\text{PO}_4)_2\text{F}_{3-y}$ (NVPFO_y) has attracted extensive attention for its high operating voltage and structural stability. In order to promote better performance at high rates, it appears interesting to consider the correlation between NVPFO_y's composition, morphology (size and shape) and electrochemical properties. Here, solvothermal syntheses were considered in order to obtain a series of NVPFO_y compounds showing different morphologies (such as nanospheres, flakes, cylindrical aggregates or desert-roses) by playing on different synthesis parameters like water/ethanol ratio,

stoichiometry of the precursors' mixture, heating rate, and the presence or not of a surfactant. Four compounds presenting different morphology have been fully characterized by X-ray diffraction, scanning electron microscopy, transmission electron microscopy, infrared, NMR and XPS spectroscopies. Their electrochemical properties are studied using electrodes rich in active material in order to better observe the influence of the morphology on the energy storage performance and are compared to those of $\text{Na}_3\text{V}_2(\text{PO}_4)_2\text{F}_3$ and $\text{Na}_3\text{V}_2(\text{PO}_4)_2\text{FO}_2$ reference materials obtained by solid-state synthesis and with shapeless morphology.

1. Introduction

Nowadays, lithium-ion batteries (LIBs) are widely used in mobile phones, laptops, electric vehicles, and energy storage stations.^[1] However, in the context of today's rapid development of electric vehicles and the increasing demand of energy storage devices for grid application, the uneven distribution of lithium resources in the earth's crust raises concerns about its stable cost and supply. Among the possible alternative technologies, sodium-ion battery is considered to be currently the most

reliable and environmentally friendly one. The very high abundance, wide distribution and low cost of sodium conjugated to similar working principle as that of already commercialized LIBs, contribute to a rapid development of sodium-ion batteries.^[2,3] These last years, a range of layered metal oxide and polyanionic materials have been intensively investigated as positive electrode materials.^[4–9] Among the polyanionic ones, the NASICON $\text{Na}_3\text{V}_2(\text{PO}_4)_3$ and the sodium vanadium oxyfluoride phosphate family, $\text{Na}_3\text{V}^{3+}_{2-y}\text{V}^{4+}_y(\text{PO}_4)_2\text{F}_{3-y}\text{O}_y$ (NVPFO_y) ($0 \leq y \leq 2$), have attracted extensive attention for their structural stability and low volume change upon the reversible extraction of 2Na^+ per formula unit. However, due to the higher reversible capacity and average extraction potential (128 mAh g^{-1} vs. 118 mAh g^{-1} and $\sim 3.9 \text{ V}$ vs. 3.4 V (vs. Na^+/Na) for $\text{Na}_3\text{V}_2(\text{PO}_4)_2\text{F}_3$ and $\text{Na}_3\text{V}_2(\text{PO}_4)_3$, respectively), NVPFO_y family exhibits stronger perspective in term of application.^[10–16] For instance, Broux et al. reported excellent long-term cycling stability and high-rate performance for prototype cells made of carbon coated $\text{Na}_3\text{V}_2(\text{PO}_4)_2\text{F}_3$ versus hard carbon.^[10] Their 75 Wh kg^{-1} 18650 prototype cells exhibited 80% of capacity retention after 4000 cycles at 1 C rate.

$\text{Na}_3\text{V}^{3+}_{2-y}\text{V}^{4+}_y(\text{PO}_4)_2\text{F}_{3-y}\text{O}_y$ ($0 \leq y \leq 2$) has a three-dimensional framework built of $\text{V}_2\text{O}_8\text{F}_{3-y}\text{O}_y$ bi-octahedral units linked together by phosphate groups via oxygen atoms, and the highly mobile Na ions occupy the tunnel sites along the [110] and [1̄10] directions.^[17] The presence of isolated vanadium bi-octahedra in the structure induces a poor intrinsic electronic conductivity ($\sim 10^{-12} \text{ S cm}^{-1}$) which strongly affects the high-rate capacity retention.^[18] To face this problem, the main approaches studied in the literature consist in combining NVPFO_y with conductive carbon based material to synthesize composites or in decreasing particles size to facilitate the accessibility of electrolyte to the electrode surface and shorten

[a] R. Fang, Prof. S. Cassaignon
Sorbonne Université
CNRS Laboratoire Chimie de la Matière Condensée de Paris, LCMCP
UMR 7574
4 Place Jussieu, 75005 Paris, France
E-mail: sophie.cassaignon@sorbonne-universite.fr

[b] Dr. J. Olchowka, C. Pablos, Dr. P. S. Camacho, Prof. D. Carlier,
Dr. L. Croguennec
CNRS, Univ. Bordeaux
Bordeaux INP, ICMCB UMR 5026
33600 Pessac, France
E-mail: jacob.olchowka@icmcb.cnrs.fr

[c] C. Pablos
Laboratoire de Réactivité et de Chimie des Solides
Université de Picardie Jules Verne
CNRS-UMR 7314
F-80039 Amiens Cedex 1, France

[d] R. Fang, Dr. J. Olchowka, C. Pablos, Prof. D. Carlier, Dr. L. Croguennec,
Prof. S. Cassaignon
RS2E, Réseau Français sur le Stockage Electrochimique de l'Energie
CNRS 3459
80039 Amiens Cedex 1, France

[e] Dr. J. Olchowka, Prof. D. Carlier, Dr. L. Croguennec
ALISTORE-ERI European Research Institute
CNRS 3104
80039 Amiens Cedex 1, France

 Supporting information for this article is available on the WWW under
<https://doi.org/10.1002/batt.202100179>

ion and electron transport pathways.^[19–21] For instance, dealing with this last approach, it was shown that nanosizing carbon coated-NVPF by mechanical activation improves high rate capacity and cycling stability.^[22] Although it is well known that particle's size and morphology influence the energy storage performance and a lot of particle shapes can be obtained, such as nano or microspheres,^[23–25] hollow spheres,^[19,26,27] nano or microcubes,^[28–30] nano-flowers,^[31,32] platelets^[33] and other special morphologies,^[34–40] it is still unclear which particle's morphology allows to reach the best high-rate performance and if the synthesis method influences the electrochemical properties. Indeed, different electrode formulations, nature of electrolytes, active mass loadings, carbon coatings or conductive additives make very complicated a simple comparison between all the studies reported in the literature.

In this work, in order to learn more about the effect of particle shape on the electrochemical performance, energy-saving solvothermal method was used to prepare a series of $\text{Na}_3\text{V}^{3+}_{2-y}\text{V}^{4+}_y(\text{PO}_4)_2\text{F}_{3-y}\text{O}_y$ compounds showing different morphologies. The same precursors were used whatever the synthesis conditions in order to try to minimize the impact on the F/O composition. The electrochemical tests were performed

on electrodes rich in active material and with high mass loading to better observe the influence of the morphology by attenuating the effect of the carbon black additive, and to be close to the practical conditions. These results were compared to those obtained for $\text{Na}_3\text{V}^{3+}_{2-y}(\text{PO}_4)_2\text{F}_3$ and $\text{Na}_3\text{V}^{4+}_{2-y}(\text{PO}_4)_2\text{FO}_2$ synthesized by conventional solid-state synthesis.

2. Results and Discussions

2.1. Structural and Morphological Characterization

The XRD patterns of all compounds, presented in Figure 1a, confirm the successful syntheses of phases that belong to the $\text{Na}_3\text{V}^{3+}_{2-y}\text{V}^{4+}_y(\text{PO}_4)_2\text{F}_{3-y}\text{O}_y$ family. The lattice parameters determined from the Rietveld refinement of the XRD data, considering the structural model already described in detail in Ref. [13] are gathered in Table 1 and the results of the refinement are reported for each compound in Figure S1. Additionally, the elemental chemical analyses, determined by ICP-OES, reveal cationic ratio very close to the expected ones for this series of

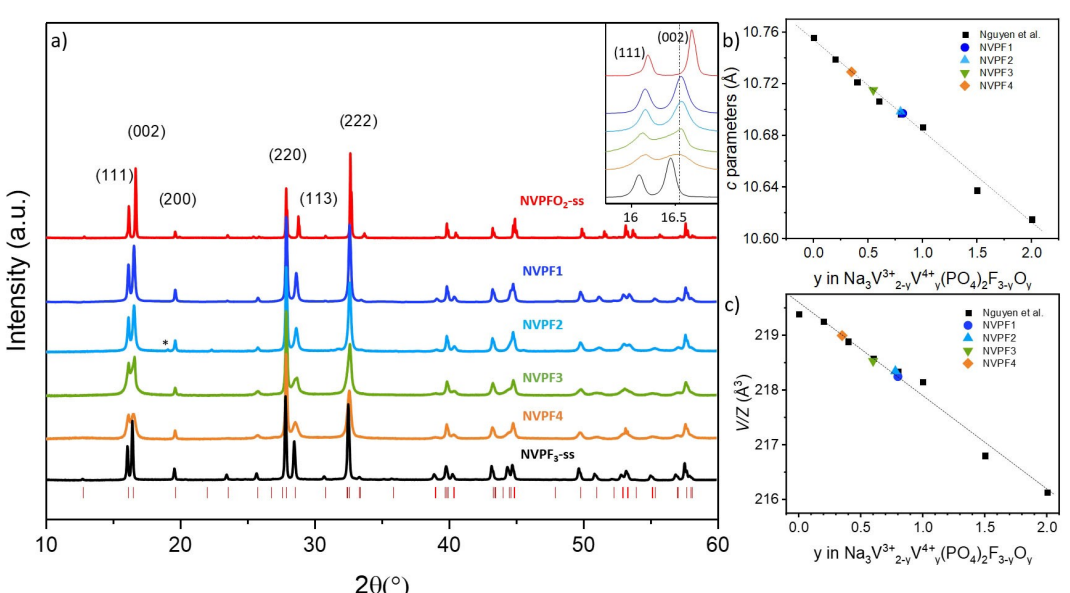


Figure 1. a) XRD patterns of all compounds: from top to bottom are respectively given that of the reference $\text{NVPFO}_2\text{-ss}$, NVPF1 , NVPF2 , NVPF3 , NVPF4 and the second reference $\text{NVPF}_3\text{-ss}$. The inset shows an enlargement of (111) and (002) reflections. The red ticks correspond to theoretical positions for $\text{Na}_3\text{V}_2(\text{PO}_4)_2\text{F}_{3-y}\text{O}_y$ as reported in ICDD 00-066-0322 and the small star for NVPF2 diagram corresponds to a reflection peak that may belong to traces of residual Pluronic acid; Comparison of b) the c cell parameters and c) V/Z values (V/Z being the cell volume per formula unit) determined by Rietveld refinement to those already reported.^[13,41,42] The dash lines give the evolution of these parameters as a function of " y " in $\text{Na}_3\text{V}_2(\text{PO}_4)_2\text{F}_{3-y}\text{O}_y$.^[13]

Table 1. Lattice parameters obtained by the Rietveld refinement, coherent domain sizes along the (220) and (002) directions and chemical composition determined for all the NVPFO_y materials.

Sample	a [Å]	b [Å]	c [Å]	V/Z [Å ³]	(220) [nm]	(002) [nm]	Formula	Space group
NVPF1	9.0331(1)	9.0374(1)	10.6970(1)	218.31(1)	61	67	$\text{Na}_3\text{V}^{3+}_{1.20}\text{V}^{4+}_{0.80}(\text{PO}_4)_2\text{F}_{2.20}\text{O}_{0.80}$	Amam
NVPF2	9.0339(1)	9.0368(1)	10.6983(1)	218.34(1)	60	56	$\text{Na}_3\text{V}^{3+}_{1.20}\text{V}^{4+}_{0.80}(\text{PO}_4)_2\text{F}_{2.20}\text{O}_{0.80}$	Amam
NVPF3	9.0316(1)	9.0344(1)	10.7150(1)	218.53(1)	55	35	$\text{Na}_3\text{V}^{3+}_{1.45}\text{V}^{4+}_{0.55}(\text{PO}_4)_2\text{F}_{2.45}\text{O}_{0.55}$	Amam
NVPF4	9.0347(2)	9.0387(2)	10.7291(2)	219.00(2)	57	30	$\text{Na}_3\text{V}^{3+}_{1.65}\text{V}^{4+}_{0.35}(\text{PO}_4)_2\text{F}_{2.65}\text{O}_{0.35}$	Amam
$\text{NVPFO}_2\text{-ss}$	9.0330(1)	9.0330(1)	10.6137(2)	216.51(1)	60	65	$\text{Na}_3\text{V}_2(\text{PO}_4)_2\text{FO}_2$	$P4_3/mn$
$\text{NVPF}_3\text{-ss}$	9.0304(1)	9.0437(1)	10.7490(1)	219.46(1)	76	101	$\text{Na}_3\text{V}_2(\text{PO}_4)_2\text{F}_3$	Amam

$\text{Na}_3\text{V}^{3+}_{2-y}\text{V}^{4+}_y(\text{PO}_4)_2\text{F}_{3-y}\text{O}_y$ compounds ($\text{Na}/\text{V}/\text{P}=1.5/1/1$) (Table 2).

The determination of the cell parameters allows a good estimation of the O^{2-} for F^- substitution: the smaller the cell volume and c cell parameter (experimentally observed with a shift of (002) diffraction peak to higher diffraction angles), the higher is the content in oxygen in $\text{Na}_3\text{V}_2(\text{PO}_4)_2\text{F}_{3-y}\text{O}_y$.^[13,42-44] Indeed, the substitution of O^{2-} for F^- induces the vanadium oxidation (V^{3+} to V^{4+}) for charge compensation, along with the formation of vanadyl bonds ($\text{V}=\text{O}^{2+}$) and leads to a solid solution between the two end-members, $\text{Na}_3\text{V}^{3+}_{2-y}(\text{PO}_4)_2\text{F}_3$ and $\text{Na}_3\text{V}^{4+}_y\text{O}_2(\text{PO}_4)_2\text{F}$. As the vanadyl bonds are localized along the c -axis (Figure S2) (in the *Amam* space group), the replacement of long ionic $\text{V}-\text{F}$ bonds (2 Å) by short covalent $\text{V}=\text{O}$ bonds (~1.6 Å) induces a decrease of the c cell parameter. As shown in Figures 1(b,c) and S3, the compounds NVPF1 and NVPF2 are characterized by the higher oxygen contents, similar for both of them and in good agreement with the chemical composition $\text{Na}_3\text{V}^{3+}_{1.20}\text{V}^{4+}_{0.80}(\text{PO}_4)_2\text{F}_{2.20}\text{O}_{0.80}$ (i.e., $y=0.8$). The compound NVPF3 is less oxidized and shows the composition $\text{Na}_3\text{V}^{3+}_{1.45}\text{V}^{4+}_{0.55}(\text{PO}_4)_2\text{F}_{2.45}\text{O}_{0.55}$ ($y=0.55$), whereas the compound NVPF4 is even less oxidized with the composition $\text{Na}_3\text{V}^{3+}_{1.65}\text{V}^{4+}_{0.35}(\text{PO}_4)_2\text{F}_{2.65}\text{O}_{0.35}$ ($y=0.35$) (Table 1). It appears thus that a partial oxidation of the V^{3+} precursor takes place in the conditions used during the solvothermal syntheses due to presence of oxidative solvent. It clearly shows the difficulty to control the oxygen content (vanadium oxidation state) by using solvothermal approach.^[45]

Further, the presence of vanadyl bonds ($\text{V}=\text{O}$) and mixed $\text{V}^{3+}/\text{V}^{4+}$ valence state (also written as $\text{V}^{3+}/(\text{V}=\text{O})^{2+}$) were confirmed by infrared, ^{23}Na NMR and X-Ray photoelectron spectroscopies. The IR spectra of all these compounds obtained by solvothermal syntheses are compared in Figure 2(a). They exhibit vibrational bands at 680 cm^{-1} and 1080 cm^{-1} , which respectively correspond to the stretching modes of vanadium oxygen bond $v(\text{V}-\text{O})$ and phosphate groups $v(\text{PO}_4^{3-})$. Additionally, the spectra reveal two peaks at ~910 and 940 cm^{-1} characteristic of the vibrations generated by a vanadyl bond (Figure 2a).^[13,46,47] These peaks are, as expected, very intense for NVPFO₂-ss and not observed for NVPF₃-ss, characterized for this latter by the composition $\text{Na}_3\text{V}^{3+}_{2}(\text{PO}_4)_2\text{F}_3$ (i.e., without any vanadyl bond ($\text{V}=\text{O}^{2+}$)).

The ^{23}Na ss-NMR spectra recorded for all compounds are given in Figure 2(b). Three main signals can be detected at ~70 ppm, ~100 ppm and ~140 ppm and indicate the presence of hyperfine interactions between the ^{23}Na nuclei and the paramagnetic $\text{V}^{3+}, \text{V}^{4+}$ ions present in their close environments. According to previous works, the more positively shifted signal is attributed to the presence of two V^{3+} in close vicinity with a Na^+ ($\text{Na}(\text{OV}^{3+})_2$ environment) whereas the lower Fermi contact shift at ~70 ppm corresponds to the interaction of two V^{4+}

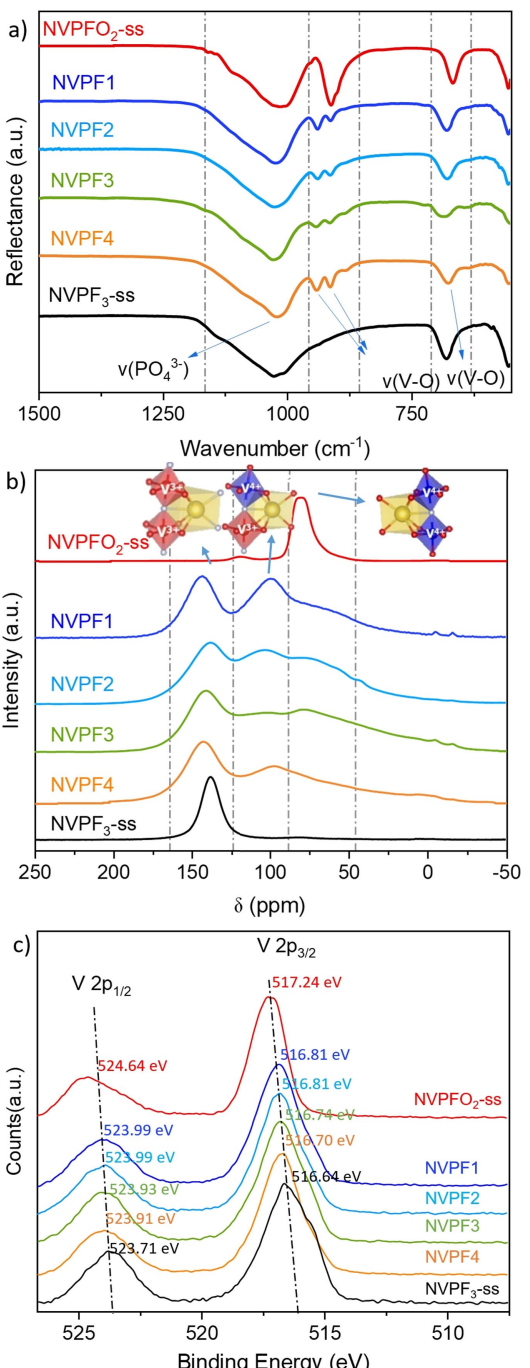


Figure 2. a) Comparison of the IR spectra of all the studied NVPFO_y materials in the wavenumber range of $550\text{--}1500\text{ cm}^{-1}$. b) ^{23}Na ss-NMR spectra recorded for all compounds. The fitting results of ^{23}Na ss-NMR are reported Figure S4. c) XPS spectra of V 2p orbital.

with a Na^+ ($\text{Na}(\text{OV}^{4+})_2$ environment).^[42-44,48] The intermediate signal at ~100 ppm corresponds to a $\text{Na}(\text{OV}^{4+})(\text{OV}^{3+})$ local environment. The presence of these three broad signals for NVPF1, NVPF2, NVPF3 and NVPF4 thus confirms the mixed $\text{V}^{3+}/\text{V}^{4+}$ vanadium oxidation state.^[48,49] Moreover, by fitting the spectra, we found the presence of a 4th signal with an even lower paramagnetic shift (between 20–39 ppm, as shown in Figure S4), which may originate from environment where Na^+

Table 2. Cationic ratio determined by ICP-OES

ICP	NVPF1	NVPF2	NVPF3	NVPF4
Na/V/P	1.49:1:1.00	1.47:1:0.97	1.39:1:1.10	1.46:1:1.01

is in close interaction with only one vanadium. These environments could come from the surface defects probably enhanced by the nanosizing of the particles, as we will see in the next part. Nevertheless, the higher intensity of the signal measured at ~ 140 ppm compared to those at ~ 100 and ~ 70 ppm observed for NVPF4 and NVPF3, indicates that the vanadium average oxidation degree is closer to V^{3+} and confirms the trend composition determined by XRD.

The vanadium oxidation state has also been evaluated by XPS analyses (Figure 2c). The V2p spectrum of $NVPFO_2$ -ss reference exhibits two broad components at 517.24 and 524.77 eV coming from $V2p_{3/2}$ and $V2p_{1/2}$ transitions, respectively, and which are consistent with results expected for V^{4+} in such polyanionic materials.^[35] On the other hand, NVPF3-ss demonstrates that the binding energies of $V2p_{3/2}$ and $V2p_{1/2}$ are located at 516.49 and 523.71 eV, in good agreement with a vanadium in its trivalent state in such polyanionic materials.^[35] All the compounds obtained by solvothermal reaction have $V2p_{3/2}$ and $V2p_{1/2}$ binding energies in between those of the two references, confirming the mixed V^{3+}/V^{4+} valence state and in very good agreement with the vanadium mean oxidation state deduced from changes in the cell parameters determined from XRD patterns analysis.

As it can be seen in the SEM and TEM images (Figure 3, and for more details Figures S5 and S6 in Supporting Information),

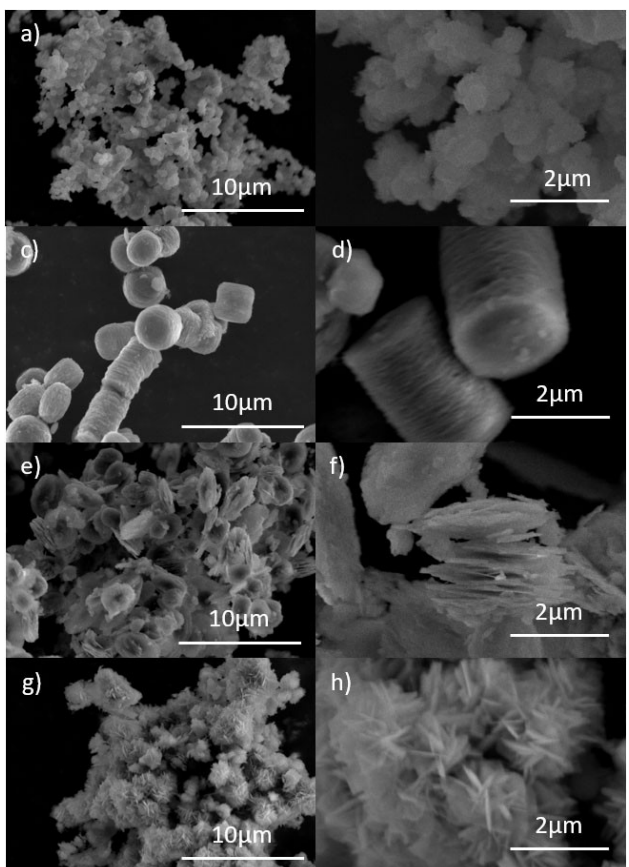


Figure 3. SEM images of all studied materials: a, b) NVPF1, c, d) NVPF2, e, f) NVPF3, and g, h) NVPF4.

various particle morphologies generated by different aggregation/organization of similar nanoscale primary particles (Table 1) were successfully obtained by slightly adjusting synthesis conditions while maintaining the same synthesis precursors (Table 4). Indeed, increasing the amount of phosphoric acid does not only change the acidity of the reaction medium, but also modify the complexation process of the particle surface, which allows to stabilize a large extent of different particle's morphologies. The addition of the surfactant Pluronic F127 also allows to control the growth of the primary particles and the way they aggregate to form the final cylindrical-shape secondary particles. Ethanol, with its smaller surface tension compared to water, also allows to modify the shape of the primary and secondary particles by playing with the concentration of ethanol in water/ethanol solutions. Finally, the slower ramp-up curve allows for a more continuous change in temperature in the reaction media and thus, a more homogeneous nucleation and aggregation for the formation of controlled particles' size.

Synthesis using stoichiometric ratio (i.e., according to the molar ratio of 1 for the vanadium precursor, 1.5 for sodium fluorine and 1 for phosphoric acid) reacted at 180 °C for ten hours leads to the formation of spherical nanoparticles of around 300 nm (NVPF1, Figures 3a,b and S6). Under the influence of Pluronic F127 surfactant in a more concentrated ethanol solution media, and with a gentler heating profile, the particles grow into micron-sized cylindrical aggregates composed of flakes around 2–3 μ m (NVPF2, Figures 3c,d and S6). Interestingly, despite different synthesis conditions used to prepare NVPF1 and NVPF2, a negligible impact was observed on their chemical composition and on their coherent domains' size, which was determined using Scherrer formula (Table 1). The addition of surfactant certainly orients the aggregation of primary particles to the stacking of the basal faces, which show a smaller surface energy. On the contrary, increasing the molar ratio of H_3PO_4 and NaF versus that of vanadium acetylacetone affects both the oxygen content and the morphology as shown by the comparison of NVPF1 and NVPF4. The spherical nanoparticles of NVPF1 become micrometric aggregates similar to desert roses for NVPF4 (Figures 3g,h and S5), and the excess of phosphoric acid is most probably limiting the vanadium oxidation during the synthesis of the latter. Furthermore, in the absence of Pluronic F127 conjugated to a higher amount of H_3PO_4 , the aggregates of flakes observed for NVPF2 lose their cylindrical-shape microstructure to form rounded flake (around 2–3 μ m length) for NVPF3 (Figures 3e,f). Finally, an excess of NaF and H_3PO_4 used for the synthesis of NVPF3 and NVPF4 leads to the formation of small coherent domains along the [002] direction close to 30–35 nm, whereas larger ones are observed for NVPF1 and NVPF2 with ~ 65 nm and ~ 55 nm respectively (Table 1). It is worth mentioning that platelet-like shape particles are obtained with different thicknesses for NVPF2 (ca. 100 nm), NVPF3 (ca. 100 nm) and NVPF4 (ca. 50 nm), and that all the morphologies prepared in these solvothermal conditions are very different from that observed for $Na_3V_2-y(PO_4)_2F_{3-y}O_y$ synthesized by solid state method and showing big and irregular aggregates made of ill-defined particles fused

together (Figures S5). The results of specific surface area (SSA) measured for all compounds are given in Table S9 and the SSA trend fits well to the different morphologies that are compared.

In order to study further the morphology of the different samples, high resolution TEM was performed to determine the flakes' orientation in NVPF3 and NVPF4 (Figure 4). The flakes observed in NVPF3 were found to exhibit (00l) crystallographic planes through fringe calculation, in good agreement with an orientation of the nanoplatelets along the c-axis (Figure 4a). As the Na^+ ions diffuse in channels situated in the (ab) plane, perpendicular to the orientation of the primary particles, it could be expected that the stacking of nanosheets, forming the flakes, would make Na^+ insertion/extraction difficult.^[11] Similarly, the platelets that compose the sand-roses are also orientated along (00l) planes, however this time their special aggregation leads to an easy access to the nanoplatelets' surface and should thus favor good Na^+ diffusion (Figure 4b). The orientation determined for the platelets is in good agreement with the work of Yi et al. that also found 2D NVPF platelets oriented along (00l) planes through fringe calculation.^[50]

2.2. Electrochemical Properties

The electrochemical behavior and reaction kinetics were investigated for the four samples by galvanostatic charge/discharge (GCD) experiments and cyclic voltammetry (CV) in coin-type half-cells versus metallic Na, and were compared to those obtained for NVPF₃-ss and NVPFO₂-ss. Although the materials prepared by solvothermal approach are not carbon coated, electrodes were prepared such as to contain a high mass loading ($\sim 6 \text{ mg cm}^{-2}$), with 88 wt% of active material, 7 wt% of carbon and 5 wt% of PVDF as binder, in order to be close to practical conditions and better observe the influence of the materials' morphology. Figure 5(a-d) shows the GCD profiles of the 1st, 2nd and 5th cycles obtained at a cycling rate of C/20 in the potential range 2.5–4.3 V vs. Na^+/Na . As expected, due to the mixed valence state of vanadium with the presence of V^{3+} and $(\text{V}=\text{O})^{2+}$ in NVPF1, NVPF2, NVPF3 and NVPF4, their electrochemical curves are characterized by two sloping "plateaus" showing thus the succession of two solid-solution composition domains upon Na^+ extraction/insertion. On the

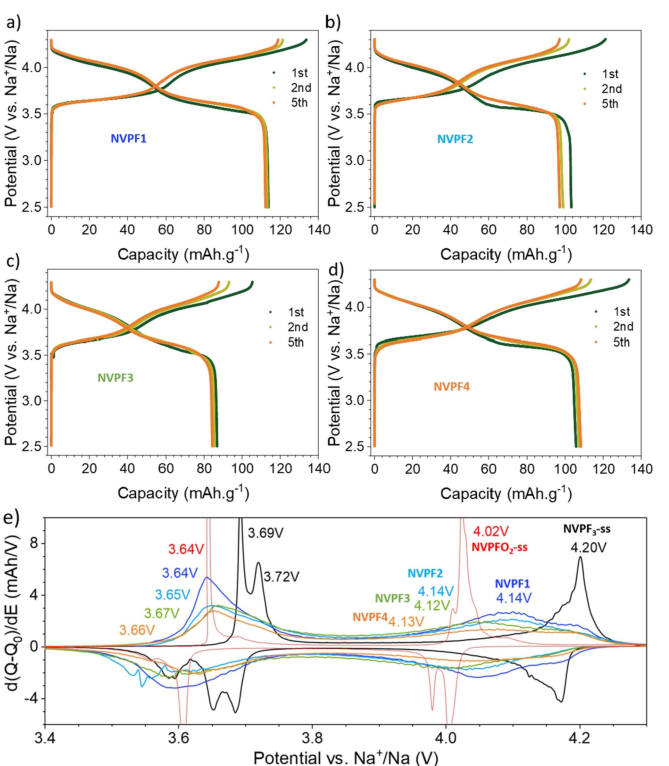


Figure 5. a-d) Galvanostatic charge and discharge curves obtained for all the NVPFO_y materials at the cycling rate of C/20. e) Associated derivative curves of the 5th cycles.

contrary, the NVPF₃-ss and NVPFO₂-ss (Figure S8) exhibit well defined plateaus revealing the reversible extraction of Na^+ ions through a succession of biphasic reactions mainly.^[17] The difference between these desodiation mechanisms can be clearly identified on the first derivative curve of the 5th cycles (Figure 5e). The broad peaks confirm the S-shape profile (i.e., solid solution type reaction) and the sharp and intense peaks observed at 3.69, 3.72, 4.20 V for NVPF₃-ss and 3.64, 4.02 V for NVPFO₂-ss agree with successive biphasic reactions (Figures 5e and S7). Figure 5(e) also reveals that the average oxidation potentials are similar for the four materials prepared by solvothermal syntheses (~3.65 and ~4.13 V), showing thus that the oxygen content has a very limited impact on the Na^+ extraction potential in the composition range $0.35 \leq y \leq 0.8$.

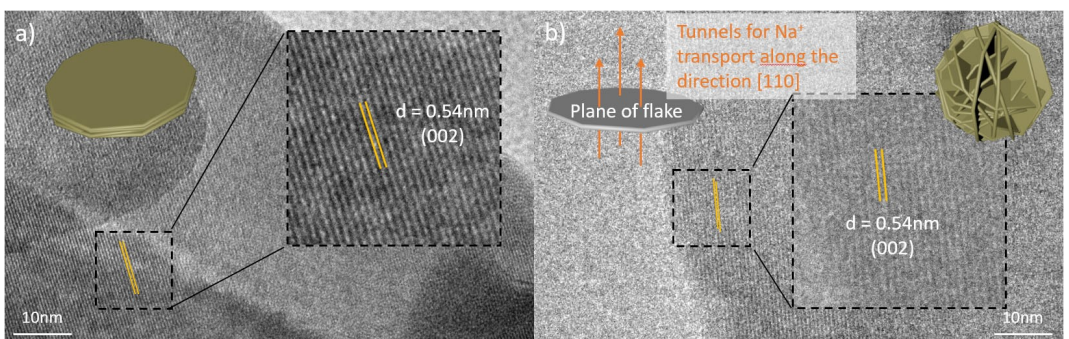


Figure 4. TEM images of the flakes of a) NVPF3 and b) NVPF4 with 3D models and schematic.

with y in $\text{Na}_3\text{V}^{3+}_{2-y}\text{V}^{4+}_y(\text{PO}_4)_2\text{F}_{3-y}\text{O}_y$. As shown by Nguyen et al., the redox couples $\text{V}^{4+}/\text{V}^{3+}$ and $(\text{V}=\text{O})^{3+}/(\text{V}=\text{O})^{2+}$ are activated simultaneously upon Na^+ extraction in these four electrode materials.^[51] On the contrary, the absence of covalent vanadyl bonds in NVPF₃-ss leads to higher average Na^+ extraction potential (~ 3.7 and ~ 4.2 V). At C/20 all the materials display low polarization in Na cells, however NVPF1 and NVPF4 exhibit higher specific capacity: 114 mAh g⁻¹ and 108 mAh g⁻¹ respectively (as determined from the 2nd cycle), versus 99 and 86 mAh g⁻¹ for NVPF3 and NVPF2 and 86 and 70 mAh g⁻¹ for NVPF₃-ss and NVPO₂-ss (Figures 6 and S8). It seems that the stacking of nanosheets into flakes (NVPF3) or into cylinders (NVPF2) is detrimental to performance as expected from HRTEM analyses. Indeed, the sodium diffusion channels are perpendicular to their basal surface and their random stacking (no oriented aggregation) limits sodium insertion. Indeed, contrary

to nanosphere (NVPF1) or nanoflower (NVPF4) morphologies, this stacking may prevent a good contact between the primary particles and the electrolyte that limits the participation of the "active material" to the electrochemical activity. To get more information, the materials were tested at different current densities, from C/20 up to 2 C (Figure 7a). Once again, NVPF1 shows the best specific capacities at high rates, far ahead NVPF4 this time. This implies that nanosphere morphology (NVPF1) allows reaching better ionic and/or electronic kinetics than the desert rose morphology composed of randomly oriented flakes (NVPF4). It is also interesting to notice that NVPF3 shows a better capacity retention than NVPF2 at higher rate than C/5, which may suggest that further micro-structuration of flakes into cylindrical aggregates prevents a good ionic diffusion. Indeed, the random orientation of the stacking flakes is more likely to cause misalignment of the sodium pathway at

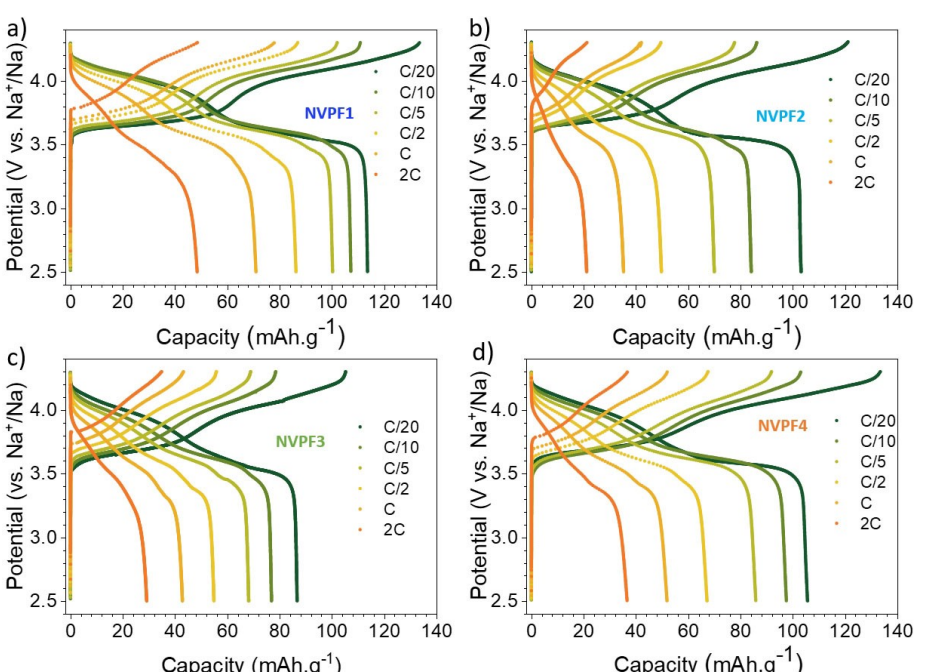


Figure 6. a-d) Charge and discharge curves of NVPO_y materials at different cycling rates, from C/20 to 2 C.

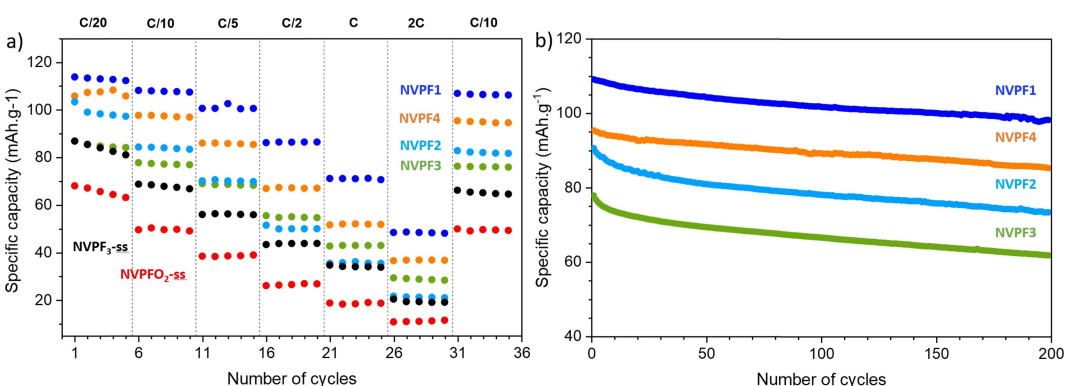


Figure 7. a) Rate capabilities obtained for all the studied materials at various rates from C/20 to 2 C. b) Cycling performance of all the NVPO_y materials prepared without any carbon coating, comparison at a current rate of C/10.

the junction of the flakes and thus slow down the Na^+ transport. Similar observation was reported by Shen et al., who observed that discharge capacity becomes higher when the microstructure becomes looser.^[19] It is also noted that NVPF1 and NVPF2 determined with the same chemical composition $\text{Na}_3\text{V}^{3+}_{1.20}\text{V}^{4+}_{0.80}(\text{PO}_4)_2\text{F}_{2.20}\text{O}_{0.80}$ exhibit respectively the best and the worst high rate capacities among the nanostructured materials, which confirms the strong influence of morphology on the electrochemical performance. Compared to NVPF₃-ss and NVPFO₂-ss, all the materials obtained by solvothermal method present better capacity, which highlights the great potential of the solvothermal synthesis method and the influence of the synthesis approach. Meanwhile, the less fluorinated NVPFO₂-ss presents the worst performance, suggesting the increase of O/F ratio is not the major reason for the electrochemical performance improvement of NVPF1.

Finally, the recovering of the original performance at C/10 after cycling at high rates reveals the good structural stability for all phases and implies that the capacity decrease upon higher current comes from limited kinetics (Figure 7a).

According to Figure 7(b), all the compounds show a capacity retention higher than 80% after 200 cycles at C/10 and an initial specific capacity higher than 80 mAh g^{-1} . NVPF1 showing a controlled granulometry with independent particles of 300 nm delivers the best performance, with an initial specific capacity of 110 mAh g^{-1} and a capacity retention of about 91% after 200 cycles.

In order to investigate more deeply the influence of the morphology on the ionic diffusion, CV analysis was used to analyze the Na^+ migration kinetics in NVPFO_y materials at various scan rates from 0.025 to 0.8 mVs^{-1} and in the potential range 2.5–4.3 V vs. Na^+/Na , the upper cut-off voltage being limited to 4.3 V to avoid any possible electrolyte degradation. For all the materials, two reversible oxidation peaks, corresponding to the two pseudo-plateaus observed in GCD mode, can be observed at low scan rate. It can be seen that the height and area of these peaks continuously increase with the increasing rate. Simultaneously the polarization also increases which shifts the high potential oxidation peak out of the selected electrochemical window. Thus, the second oxidation/reduction was not complete and only the behavior of the first oxidation named O1 and its corresponding reduction (R₁) was further analyzed. Figure 8 illustrates the evolution of the peak current (i_0) versus the square root of the scan rate ($v^{1/2}$). The linear profiles demonstrate excellent fitting results and indicate that the electrochemical reactions of all the materials are based on diffusion-controlled processes for Na^+ intercalation/deintercalation. Based on the above CV measurements and linear fitting results, the apparent ion diffusion coefficient (Table 3)

can be determined from the Randles-Sevcik equation (see Supporting Information Part S11).

First of all, it can be seen that the diffusion coefficient determined upon reduction process is always lower than that upon oxidation reaction, which shows that Na^+ can be more easily extracted than re-intercalated. The one determined for NVPF1 presents the highest diffusion coefficient ($1.60 \times 10^{-11} \text{ cm}^2 \text{s}^{-1}$), nearly one order of magnitude higher than that for NVPFO₂-ss reference (Figure S10), and reveals very promising diffusion abilities considering the absence of coating and the electrode formulation chosen. Then, NVPF4, NVPF2 and NVPF3 possess diffusion coefficient of 1.22×10^{-11} , 9.99×10^{-12} and $8.82 \times 10^{-12} \text{ cm}^2 \text{s}^{-1}$ respectively. These values are consistent with those reported in literature and even sometimes higher than for carbon-coated NVPF materials^[19,23,52,53] (e.g., $6.366 \times 10^{-12} \text{ cm}^2 \text{s}^{-1}$ for NVPF@C reported by Shen et al.^[23]). Finally, these results confirm the energy storage performance measured previously and demonstrate that the nanosphere morphology of NVPF1 facilitates the ionic diffusion and generates thus better kinetics compared to those of agglomeration of platelets within flakes, sand-rose flowers or cylinders' morphologies.^[10,54]

3. Conclusions

A series of $\text{Na}_3\text{V}^{3+}_{2-y}\text{V}^{4+}_y(\text{PO}_4)_2\text{F}_{3-y}\text{O}_y$ materials with different morphologies (nanosphere, micrometric flake, cylindrical agglomerate and sand-rose) were obtained by controlling the precursors' molar ratio, the ethanol concentration in the water/ethanol mixture and the heating rate during solvothermal syntheses, but also by adding a surfactant. Through a series of thorough characterization, the anionic composition in oxygen and fluorine and the structure were determined for the different compounds, found to belong to the $\text{Na}_3\text{V}^{3+}_{2-y}\text{V}^{4+}_y(\text{PO}_4)_2\text{F}_{3-y}\text{O}_y$ family with $0.35 \leq y \leq 0.8$. The electrochemical measurements disclose that the O/F ratio has a limited influence on the average oxidation potential within the composition range $0.35 \leq y \leq 0.8$ in $\text{Na}_3\text{V}^{3+}_{2-y}\text{V}^{4+}_y(\text{PO}_4)_2\text{F}_{3-y}\text{O}_y$, whereas the V^{3+} -rich $\text{Na}_3\text{V}_2(\text{PO}_4)_2\text{F}_3$ compound exhibits a higher average potential of $\sim 0.1 \text{ V}$ due to the absence of covalent vanadyl bonds. This study has demonstrated that particles morphology has a strong influence on the energy storage performance. It was shown that the misaligned stacking of nanosheets grown perpendicularly to the Na^+ diffusion channels prevents for a fast Na^+ diffusion. On the other hand, sand rose and especially nanosphere morphologies, which allow for an easy access to the Na^+ diffusion channels situated in the (ab) crystallographic plane, exhibit the best high rate performance and should be favored in future works.

Table 3. Diffusion coefficients determined for the four different samples.

Reaction	$D [\text{cm}^2 \text{s}^{-1}]$	NVPF1	NVPF2	NVPF3	NVPF4
O1	1.60×10^{-11}	9.99×10^{-12}	8.82×10^{-12}	1.22×10^{-11}	
R1	9.46×10^{-12}	4.72×10^{-12}	4.39×10^{-12}	6.30×10^{-12}	

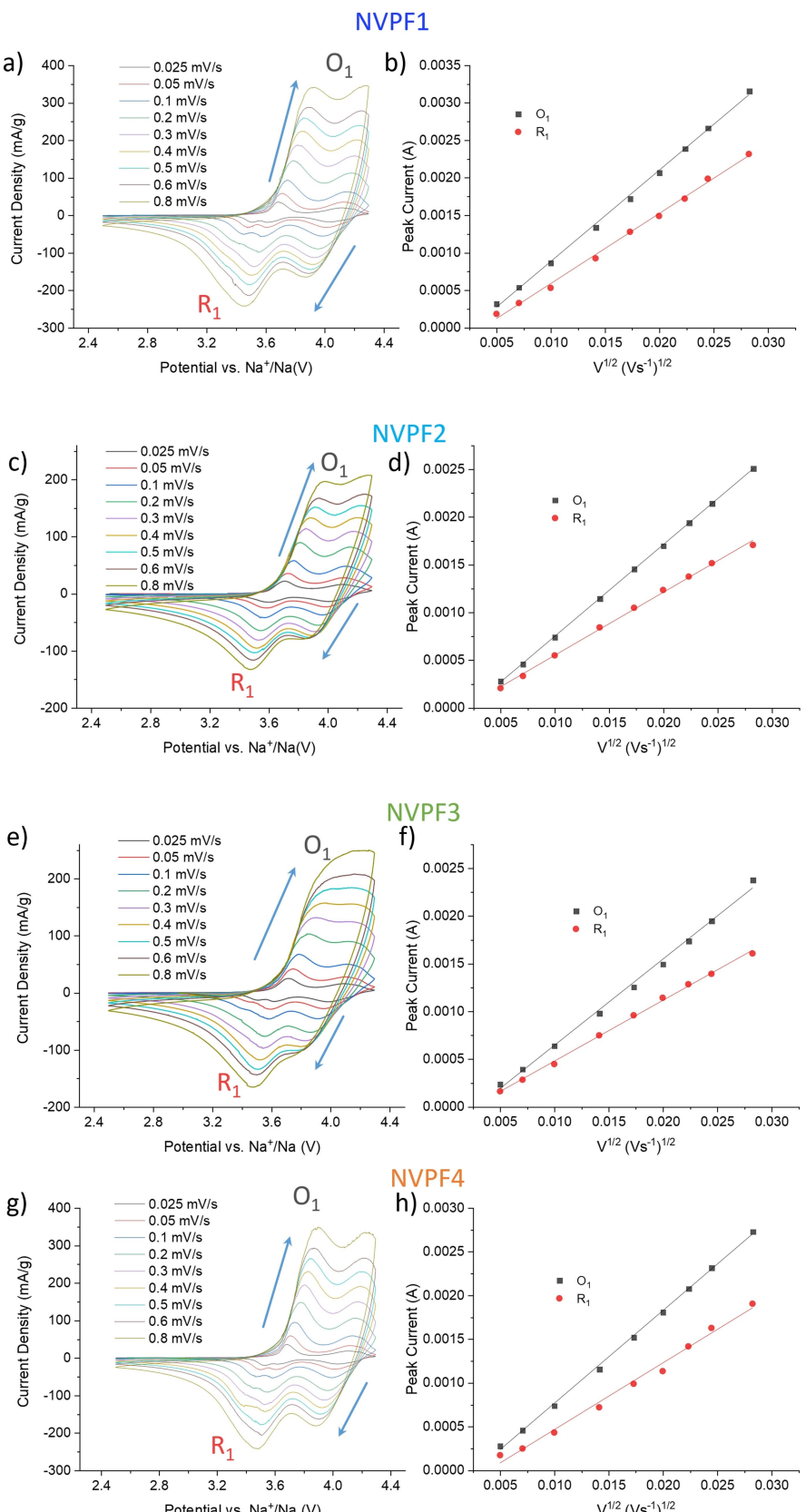


Figure 8. a-h) CV curves at different scan rates and the corresponding linear fitting curves between the peak current (i_p) and the square root of the scan rate ($v^{1/2}$): a, b) NVPF1, c, d) NVPF2, e, f) NVPF3, g, h) NVPF4.

Table 4. Detailed synthesis method and parameters of all the studied materials.

Type	Vanadium acetylacetone	Sodium fluorine	Phosphoric acid	Water/ethanol solution	Additive	Heating rate	T [°C]	Time [h]
NVPF1	1	1.5	1	50%/50%	X	Directly in oven	180	10
NVPF2	1	1.5	1	10%/90%	Pluronic F127	1 °C min ⁻¹	180	10
NVPF3	1	1.67	1.5	10%/90%	X	0.5 °C min ⁻¹	180	10
NVPF4	1	1.67	1.5	50%/50%	X	Directly in oven	180	10

Experimental Section

Materials preparation

The $\text{Na}_3\text{V}^{3+}_{2-y}\text{V}^{4+}_y(\text{PO}_4)_2\text{F}_{3-y}\text{O}_y$ compounds were prepared by one step solvothermal reaction, by adding required amounts of vanadium acetylacetone (Sigma-Aldrich; ≥ 97%), sodium fluoride (Prolabo; 98%) and phosphoric acid (VWR; 85%). Starting from these precursors, numerous different morphologies were obtained under different synthesis conditions. In this work, four of them that exhibit homogeneous morphologies were chosen to be studied more in details. As described in Table 4, different synthesis parameters were explored: the molar ratio of the precursors (the amount of NaF and H_3PO_4 were adjusted whereas the concentration of vanadium acetylacetone was kept around 0.2 mol L⁻¹), the nature of the solution (water/ethanol mixtures), the use of the surfactant additive Pluronic F127 (Sigma-Aldrich) and the thermal treatment conditions. Indeed, the precursor solution was heated at 180 °C in a Teflon Parr autoclave, for 10 h with different heating rates (Table 4). Depending on the experimental conditions, polycrystalline powders with different green shades were recovered after several washing steps by centrifugation (first with ethanol then with distilled water), and a final drying in vacuum at 60 °C overnight. A wide variety of $\text{Na}_3\text{V}^{3+}_{2-y}\text{V}^{4+}_y(\text{PO}_4)_2\text{F}_{3-y}\text{O}_y$ compounds with different morphologies were obtained by playing on the experimental parameters. In this study, we selected four samples showing different and homogeneous morphology as well as well crystallized particles and we do not consider samples showing heterogeneous particles morphology or amorphous parts.

Besides, $\text{Na}_3\text{V}^{3+}_2(\text{PO}_4)_2\text{F}_3$ (NVPF₃-ss) and $\text{Na}_3\text{V}^{4+}_2(\text{PO}_4)_2\text{FO}_2$ (NVPFO₂-ss) material synthesized by solid state approach according to Ref. [13] and were used as references for comparison.^[13,55]

Characterization techniques

X-ray diffraction (XRD) measurements were carried out by using a BRUKER D8 ADVANCE diffractometer in θ - θ configuration, equipped with a Cu K_{α1,2} X-ray source. The acquisition was performed in the 2θ angular range of 10°–140° with a step size of 0.0197°. The Rietveld refinements were performed using the FullProf Suite.^[56]

Scanning electron microscopy (SEM) images were taken without any conductive deposition by a Hitachi Model S-3400 N microscope.

Transmission electron microscopy (TEM) was carried out with the Tecnai spirit G2 microscope.

The chemical analysis of the Na, P and V contents was performed by inductively coupled plasma-optical emission spectroscopy (ICP-OES) using a Varian Model 720-ES spectrometer, after a complete dissolution of the powders into a concentrated hydrochloric acid (HCl) solution.

Fourier transformed infrared (FT-IR) spectra were recorded by using a PerkinElmer Spectrum 400 FT-IR/FT-NIR spectrometer in the wavenumber range of 400–4000 cm⁻¹ (mid-IR).

²³Na ss-NMR spectra were acquired using a Bruker Advance III 500WB spectrometer equipped with an 11.7 T wide bore magnet (operating at Larmor frequency of 132.3 MHz for ²³Na). Experiments were performed using a conventional 2.5 mm MAS probe with a 30 kHz MAS rate. In each case, a short pulse length of 1 μs corresponding to a selective π/8 pulse was employed. The spectral width was set to 1 MHz and the recycle delay to $D_0=0.2$ s, which was long enough to avoid T_1 saturation effects. Chemical shifts are referenced relative to an aqueous 1 mol L⁻¹ solution of NaCl solution ($\delta^{(23)\text{Na}} = 0$ ppm).

All the ²³Na ss-NMR spectra were deconvoluted using DmFIT program.^[57] In the cases the signals were very thin, individual Lorentzian peaks were used, while a combination of Gaussian-Lorentzian 0.5 were used when broaden peaks were observed.

X-ray photoelectron spectroscopy (XPS) spectra were obtained by using an Omicron Argus X-Ray photoelectron spectrometer with a 280 W electron beam power and a monochromated AlK α radiation source (1486.6 eV). Binding energies were calibrated against the C1s binding energy at 284.8 eV.

BET surface area measurements were carried out on Micromeritics ASAP 2010 after 150 °C overnight drying.

The electrochemical properties of the materials were tested in CR2032-type coin cells. The positive electrodes were prepared as a mixture containing the active material, carbon black, and polyvinylidene fluoride (PVDF) in NMP (N-Methyl-2-pyrrolidone) with the ratio of 88/7/5 (by wt%). After an hour of thorough mixing, the black ink was casted as a flat film by doctor blade on an aluminum foil and dried in an oven at 60 °C. Disks were cut, then pressed under 5 tons and finally dried overnight at 80 °C under vacuum. A homemade electrolyte containing a 1 mol L⁻¹ solution of NaPF₆ (Strem Chemical; 99%) in ethylene carbonate and dimethyl carbonate (EC/DMC = 1/1) with 2 wt% of fluoroethylene carbonate (FEC) was used for all the electrochemical tests. The assembled cells were cycled in galvanostatic mode, from C/20 to 2 C cycling rates between 2.5 and 4.3 V vs. Na⁺/Na. The theoretical capacity being 128 mA h g⁻¹ (corresponding to 2Na⁺ reversibly extracted from NVPF), the rate C/20 corresponds to the exchange of 2Na⁺ in 20 h. The electrodes have a typical active mass loading around 6 mg cm⁻².

Acknowledgement

The authors thank the Materials Physics and Chemistry Doctoral School (ED397) of Sorbonne University for the funding of Runhe FANG's PhD thesis, as well as the financial support of Région Nouvelle Aquitaine, of the French National Research Agency (STORE-EX Labex Project ANR-10-LABX-76-01) and of the European Union's Horizon 2020 research and innovation program

under grant agreement No 875629 (NAIMA project). The authors also thank Emmanuel PETIT, Cathy DENAGE, Eric LEBRAUD (ICM CB) and Antoine MICHE (Sorbonne University) for their technical support.

Conflict of Interest

The authors declare no conflict of interest.

Keywords: morphology • design • Na-ion batteries • $\text{Na}_3\text{V}_2(\text{PO}_4)_2\text{F}_3$ • $\text{Na}_3(\text{VO})_2(\text{PO}_4)_2\text{F}$ • polyanions • synthesis design

- [1] J. B. Goodenough, Y. Kim, *Chem. Mater.* **2010**, *22*, 587–603.
- [2] Y. S. Hu, S. Komaba, M. Forsyth, C. Johnson, T. Rojo, *Small Methods* **2019**, *3*, 2–3.
- [3] I. Hasa, S. Mariyappan, D. Saurel, P. Adelhelm, A. Y. Koposov, C. Masquelier, L. Croguennec, M. Casas-Cabanas, *J. Power Sources* **2021**, *482*, 228872.
- [4] B. V. Rami Reddy, R. Ravikumar, C. Nithya, S. Gopukumar, *J. Mater. Chem. A* **2015**, *3*, 18059–18063.
- [5] F. Lalèvre, V. Seznec, M. Courty, R. David, J. N. Chotard, C. Masquelier, *J. Mater. Chem. A* **2015**, *3*, 16198–16205.
- [6] A. Ponrouch, R. Dedryvère, D. Monti, A. E. Demet, J. M. Ateba Mba, L. Croguennec, C. Masquelier, P. Johansson, M. R. Palacín, *Energy Environ. Sci.* **2013**, *6*, 2361–2369.
- [7] W. Zhou, L. Xue, X. Lü, H. Gao, Y. Li, S. Xin, G. Fu, Z. Cui, Y. Zhu, J. B. Goodenough, *Nano Lett.* **2016**, *16*, 7836–7841.
- [8] F. Chen, V. M. Kovrugin, R. David, O. Mentré, F. Fauth, J. N. Chotard, C. Masquelier, *Small Methods* **2019**, *3*, 1–9.
- [9] C. Delmas, D. Carlier, M. Guignard, *Adv. Energy Mater.* **2021**, *11*, 2001201.
- [10] T. Broux, F. Fauth, N. Hall, Y. Chatillon, M. Bianchini, T. Bamine, J. B. Leriche, E. Suard, D. Carlier, Y. Reynier, L. Simonin, C. Masquelier, L. Croguennec, *Small Methods* **2019**, *3*, 1–12.
- [11] G. Fang, Z. Wu, J. Zhou, C. Zhu, X. Cao, T. Lin, Y. Chen, C. Wang, A. Pan, S. Liang, *Adv. Energy Mater.* **2018**, *8*, 1–10.
- [12] C. Masquelier, L. Croguennec, *Chem. Rev.* **2013**, *113*, 6552–6591.
- [13] L. H. B. Nguyen, T. Broux, P. S. Camacho, D. Denux, L. Bourgeois, S. Belin, A. Iadecola, F. Fauth, D. Carlier, J. Olchowka, C. Masquelier, L. Croguennec, *Energy Storage Mater.* **2019**, *20*, 324–334.
- [14] C. Zhu, K. Song, P. A. Van Aken, J. Maier, Y. Yu, *Nano Lett.* **2014**, *14*, 2175–2180.
- [15] K. Saravanan, C. W. Mason, A. Rudola, K. H. Wong, P. Balaya, *Adv. Energy Mater.* **2013**, *3*, 444–450.
- [16] Z. Jian, L. Zhao, H. Pan, Y. S. Hu, H. Li, W. Chen, L. Chen, *Electrochem. Commun.* **2012**, *14*, 86–89.
- [17] M. Bianchini, N. Brisset, F. Fauth, F. Weill, E. Elkaim, E. Suard, C. Masquelier, L. Croguennec, *Chem. Mater.* **2014**, *26*, 4238–4247.
- [18] L. Zhu, H. Wang, D. Sun, Y. Tang, H. Wang, *J. Mater. Chem. A* **2020**, *8*, 21387–21407.
- [19] X. Shen, J. Zhao, Y. Li, X. Sun, C. Yang, H. Liu, Y. S. Hu, *ACS Appl. Energ. Mater.* **2019**, *2*, 7474–7482.
- [20] A. Criado, P. Lavela, G. Ortiz, J. L. Tirado, C. Pérez-Vicente, N. Bahrou, Z. Edoufou, *Electrochim. Acta* **2020**, *332*, 1–8.
- [21] A. R. Iarchuk, D. V. Sheptyakov, A. M. Abakumov, *ACS Appl. Energ. Mater.* **2021**, *10*, 5007–5014.
- [22] D. O. Semykina, M. A. Kirsanova, Y. M. Volkovich, V. E. Sosenkin, N. V. Kosova, *J. Solid State Chem.* **2021**, *297*, 122041.
- [23] C. Shen, H. Long, G. Wang, W. Lu, L. Shao, K. Xie, *J. Mater. Chem. A* **2018**, *6*, 6007–6014.
- [24] J. Xun, Y. Zhang, H. Xu, *Inorg. Chem. Commun.* **2020**, *115*, 107884.
- [25] J. Zhao, L. Mu, Y. Qi, Y. S. Hu, H. Liu, S. Dai, *Chem. Commun.* **2015**, *51*, 7160–7163.
- [26] A. Mukherjee, T. Sharabani, I. Perelshtein, M. Noked, *Batteries & Supercaps* **2020**, *3*, 52–55; *Supercaps* **2020**, *3*, 52–55.
- [27] P. Du, K. Mi, F. Hu, X. Jiang, D. Wang, X. Zheng, *New J. Chem.* **2020**, *44*, 12985–12992.
- [28] Y. Cai, X. Cao, Z. Luo, G. Fang, F. Liu, J. Zhou, A. Pan, S. Liang, *Adv. Sci. 2018*, *5*, DOI 10.1002/advs.201800680.
- [29] H. Jin, J. Dong, E. Uchaker, Q. Zhang, X. Zhou, S. Hou, J. Li, G. Cao, *J. Mater. Chem. A* **2015**, *3*, 17563–17568.
- [30] C. Zhu, C. Wu, C. C. Chen, P. Kopold, P. A. Van Aken, J. Maier, Y. Yu, *Chem. Mater.* **2017**, *29*, 5207–5215.
- [31] A. Mukherjee, T. Sharabani, R. Sharma, S. Okashy, M. Noked, *Batteries & Supercaps* **2020**, *3*, 510–518; *Supercaps* **2020**, *3*, 510–518.
- [32] Y. Qi, L. Mu, J. Zhao, Y. S. Hu, H. Liu, S. Dai, *J. Mater. Chem. A* **2016**, *4*, 7178–7184.
- [33] J. Olchowka, L. H. B. Nguyen, E. Petit, P. S. Camacho, C. Masquelier, D. Carlier, L. Croguennec, *Inorg. Chem.* **2020**, *59*, 17282–17290.
- [34] Y. Qi, J. Zhao, C. Yang, H. Liu, Y.-S. Hu, *Small Methods* **2018**, *3*, 1800111.
- [35] Z. Tong, Y. Qi, J. Zhao, L. Liu, X. Shen, H. Liu, *Waste Biomass Valorization* **2018**, *11*, 2201–2209.
- [36] Y. Hou, K. Chang, Z. Wang, S. Gu, Q. Liu, J. Zhang, H. Cheng, S. Zhang, Z. Chang, Z. Lu, *Sci. China Mater.* **2019**, *62*, 474–486.
- [37] Y. Qi, L. Mu, J. Zhao, Y. S. Hu, H. Liu, S. Dai, *Angew. Chem. Int. Ed.* **2015**, *54*, 9911–9916; *Angew. Chem.* **2015**, *127*, 10049–10054.
- [38] M. Xu, L. Wang, X. Zhao, J. Song, H. Xie, Y. Lu, J. B. Goodenough, *Phys. Chem. Chem. Phys.* **2013**, *15*, 13032–13037.
- [39] J. Z. Guo, P. F. Wang, X. L. Wu, X. H. Zhang, Q. Yan, H. Chen, J. P. Zhang, Y. G. Guo, *Adv. Mater.* **2017**, *29*, 1–8.
- [40] Z. Y. Gu, J. Z. Guo, Y. Yang, H. Y. Yu, X. T. Xi, X. X. Zhao, H. Y. Guan, X. He, X. L. Wu, *Inorg. Chem. Front.* **2019**, *6*, 988–995.
- [41] R. A. Shakoor, D. H. Seo, H. Kim, Y. U. Park, J. Kim, S. W. Kim, H. Gwon, S. Lee, K. Kang, *J. Mater. Chem.* **2012**, *22*, 20535–20541.
- [42] T. Broux, T. Bamine, F. Fauth, L. Simonelli, W. Olszewski, C. Marini, M. Ménétrier, D. Carlier, C. Masquelier, L. Croguennec, *Chem. Mater.* **2016**, *28*, 7683–7692.
- [43] Y. U. Park, D. H. Seo, H. Kim, J. Kim, S. Lee, B. Kim, K. Kang, *Adv. Funct. Mater.* **2014**, *24*, 4603–4614.
- [44] P. Serras, V. Palomares, J. Alonso, N. Sharma, J. M. López Del Amo, P. Kubiatk, M. L. Fdez-Gubieda, T. Rojo, *Chem. Mater.* **2013**, *25*, 4917–4925.
- [45] D. Semykina, O. Podgornova, N. Kosova, *Mater. Today: Proc.* **2020**, *25*, 497–500.
- [46] F. Sauvage, E. Quarez, J. M. Tarascon, E. Baudrin, *Solid State Sci.* **2006**, *8*, 1215–1221.
- [47] J. Olchowka, L. H. B. Nguyen, T. Broux, P. Sanz Camacho, E. Petit, F. Fauth, D. Carlier, C. Masquelier, L. Croguennec, *Chem. Commun.* **2019**, *55*, 11719–11722.
- [48] L. H. B. Nguyen, P. Sanz Camacho, T. Broux, J. Olchowka, C. Masquelier, L. Croguennec, D. Carlier, *Chem. Mater.* **2019**, *31*, 9759–9768.
- [49] C. Li, M. Shen, X. Lou, B. Hu, *J. Phys. Chem. C* **2018**, *122*, 27224–27232.
- [50] H. Yi, L. Lin, M. Ling, Z. Lv, R. Li, Q. Fu, H. Zhang, Q. Zheng, X. Li, *ACS Energy Lett.* **2019**, *4*, 1565–1571.
- [51] L. H. B. Nguyen, A. Iadecola, S. Belin, J. Olchowka, C. Masquelier, D. Carlier, L. Croguennec, *J. Phys. Chem. C* **2020**, *124*, 23511–23522.
- [52] Q. Liu, D. Wang, X. Yang, N. Chen, C. Wang, X. Bie, Y. Wei, G. Chen, F. Du, *J. Mater. Chem. A* **2015**, *3*, 21478–21485.
- [53] F. Li, Y. Zhao, L. Xia, Z. Yang, J. Wei, Z. Zhou, *J. Mater. Chem. A* **2020**, *8*, 12391–12397.
- [54] A. Ponrouch, E. Marchante, M. Courty, J. M. Tarascon, M. R. Palacín, *Energy Environ. Sci.* **2012**, *5*, 8572–8583.
- [55] N. Hall, S. Boulineau, L. Croguennec, S. Launois, C. Masquelier, L. Simonin, *U.S. Pat. Appl. Publ.* **2018**.
- [56] J. Rodriguez-Carvajal, *Phys. B* **1993**, *192*, 55–69.
- [57] D. Massiot, F. Fayon, M. Capron, I. King, S. Le Calvé, B. Alonso, J. O. Durand, B. Bujoli, Z. Gan, G. Hoatson, *Magn. Reson. Chem.* **2002**, *40*, 70–76.

Manuscript received: July 23, 2021

Revised manuscript received: September 17, 2021

Accepted manuscript online: October 11, 2021

Version of record online: October 28, 2021